PAPER

Check for updates

Ultra-highly stretchable and anisotropic SEBS/F127 fiber films equipped with an adaptive deformable carbon nanotube layer for dual-mode strain sensing†

Jiancheng Dong,[a] Le Li,[a] Chao Zhang, [ID] [b] Piming Ma, [ID] [a] Weifu Dong, [ID] [a] Yunpeng Huang [ID] *[a] and Tianxi Liu*[a]

Conductive elastomer composites are widely recognized as prospective strain sensing materials in soft robotics and biomedical engineering due to their high elasticity and light weight. However, achieving high-performance strain sensors with a broad sensing range and high gauge factor synchronously is still challenging due to the trade-off between sensitivity and stretchability. In this work, an anisotropic fiber film-based strain sensor with extraordinary dual-mode sensing capabilities was developed using highly aligned styrene-*block*-poly(ethylene-*ran*-butylene)-*block*-poly-styrene (SEBS)/PEO–PPO–PEO triblock copolymer (F127) fiber films as an anisotropic elastomer matrix and intimately incorporated multiwall carbon nanotubes (CNTs) as a deformable conductive coating. *Via* blending F127 with SEBS to endow the elastomer with superhydrophilicity, aligned electrospinning was subsequently employed to prepare highly stretchable and hydrophilic SEBS/F127 fiber films, followed by surface-induced assembly to obtain anisotropic CNT/SEBS/F127 composite fiber films equipped with an adaptive deformable CNT conducting layer. Attributed to the strong interfacial interaction between CNTs and the anisotropic fiber matrix, the obtained CNT/SEBS/F127 sensor exhibited excellent mechanical strength and exceptional dual-mode strain-sensing performance in terms of an ultra-broad response range (up to 1300% strain) and an ultra-high sensitivity (GF value of 3564 at 700% strain) when stretching parallel and perpendicular to the fiber alignment, respectively, as well as fast response/recover times (51 ms/71 ms in parallel, and 100 ms/100 ms in perpendicular) and great sensing stabilities (5000 stretching–releasing cycles) in both loading directions. Additionally, the CNT/SEBS/F127 strain sensor was able to detect various human motions, such as breathing, phonation and joint bending, presenting great potential in next-generation wearable electronics.

Introduction

Wearable/flexible sensing devices *e.g.* sports bands, pulse oximeters and pedometers have attracted growing research and industrial attention in recent years,[1–4] among which flexible strain/stress sensors have shown auspicious applications in multiple areas such as human–machine interfaces,[5] wearable medical devices[6] and electronic skins.[7] In general, strain sensors can be classified as capacitive,[8] triboelectric[9,10] and resistive[11] sensors depending on the sensing mechanism.

Flexible resistive strain sensors based on resistive materials are highly attractive owing to their simple structure, readily accessible processing, and high sensitivity. Desirable strain sensors for wearable devices are supposed to possess high flexibility, a broad response range, high sensitivity and long-term durability.[2] To achieve these properties simultaneously, extensive research attention has been devoted to developing conductive elastomeric composites for strain sensors because of their excellent stretchability, cost-efficiency and superior processability.[12–14] Nevertheless, the low-cost fabrication of high-performance flexible strain sensors still remains a great challenge.

Plenty of research work has been devoted to the integration of conductive nanomaterials/polymers with elastomers (*e.g.* PDMS,[15–17] TPU,[18–20] Ecoflex,[21,22] *etc.*) to improve the exhaustive sensing performance of flexible strain sensors. Metallic nanomaterials (nanoparticles and nanowires), two dimensional nanomaterials (graphene,[22] MXenes,[23] VNO,[24] *etc.*), conductive

[a]Key Laboratory of Synthetic and Biological Colloids, Ministry of Education, School of Chemical and Material Engineering, Jiangnan University, Wuxi, 214122, China. E-mail: hypjnu@jiangnan.edu.cn; txliu@jiangnan.edu.cn

[b]State Key Laboratory for Modification of Chemical Fibers and Polymer Materials, College of Materials Science and Engineering, Donghua University, Shanghai, 201620, China

† Electronic supplementary information (ESI) available. See DOI: 10.1039/d1ta04563f

18294 | *J. Mater. Chem. A*, 2021, 9, 18294–18305

This journal is © The Royal Society of Chemistry 2021

polymers (polyaniline,[25] polypyrrole[26] and PEDOT:PSS[27]), and their composites have been utilized as conductive fillers/layers to prepare high-performance wearable strain sensors. For example, a stretchable strain sensor was prepared *via* filtering highly conductive oxygen-doped vanadium nitride (VNO, $\sigma > 10^6$ S m^{-1}) nanosheets onto a PDMS film, and displayed a high GF value of 2667 but a limited detection range of 100% due to the cracking of the conducting layer under large deformation.[24] Another strain sensor based on a CNTs/PEDOT:PSS hybrid electrode exhibited the opposite performance with an extremely high sensing range of 1275% but a low GF value of 4.4.[28] To tackle this problem, conducting materials were hybridized to construct deformable conductive paths to balance the sensing range and sensitivity. For example, silver nanoparticles were used as bridging units to construct deformable graphene layers on a flexible PDMS film, and the developed strain sensor showed a significantly improved strain range compared to that of other graphene based strain sensors.[29] Despite all the progress made, there still exist many obstacles in optimizing the trade-off between high sensitivity and a wide sensing range.[30,31]

Apart from the above issues, current flexible strain sensors always suffer from the drawbacks of isotropic sensing characteristics, namely, the sensors exhibit similar resistance changes when stretching in all directions.[15,32] Isotropic strain sensors are incapable of responding independently to a poly-directional strain stimulus, which severely restricts their applications in sensing complex and multi-dimensional deformations. To settle these problems, many research studies have been conducted to fabricate strain sensors with an anisotropic signal response. Anisotropic design of a conductive layer is a straightforward method to prepare strain sensors with multi-direction sensing capabilities. For example, aligned silver nanowires,[33] carbon nanotubes,[34] graphene[35] and even carbonized crepe paper with aligned cellulose fibers[32] were utilized to fabricate anisotropic strain sensors with a fast response to complex strains from different stretching directions. Nevertheless, the preparation of these anisotropic strain sensors requires complicated fabrication procedures and costly raw materials, which limited their large-scale manufacture and practical applications. Hence, establishing a facile and cost-effective strategy to construct highly stretchable strain sensors with excellent anisotropic sensing properties is crucial in expanding the application of flexible strain sensors to diversified platforms.

The construction of anisotropic substrates is another viable approach to endow elastomer-based strain sensors with anisotropic sensing capabilities. Electrospinning is a simple and versatile technique to construct nano- and micro-fiber films with tunable fiber orientations. In this work, an ultra-highly stretchable strain sensor with remarkable anisotropic sensing performance was rationally designed and constructed *via* the tight incorporation of acidized CNTs onto aligned electrospun SEBS/F127 fiber films. The blending of F127 endows the SEBS matrix with superhydrophilicity and enhanced stretchability (maximum breaking elongation up to 1600% along the parallel direction), and acidized CNTs were then homogeneously incorporated into SEBS/F127 by a surface-induced assembly method to construct conductive CNT/SEBS/F127 composite fiber films. Attributed to the adaptive deformable CNT conducting layer derived from the strong interaction between acidized CNTs and the superhydrophilic and highly aligned fiber matrix, the obtained composite strain sensor exhibited exceptional dual-mode sensing performances including an ultra-broad working range (up to 1300% strain) in the parallel direction and an ultra-high sensitivity (maximum GF value of 3564) in the perpendicular direction, as well as fast response/recover times and great sensing stabilities (5000 stretching–releasing cycles) in both directions, making the CNT/SEBS/F127 dual-mode strain sensor a promising candidate for complex motion detection in flexible and wearable devices.

Experimental

Materials and reagents

Styrene-*block*-poly(ethylene-*ran*-butylene)-*block*-poly-styrene (SEBS, G1633) was supplied by Kraton. PEO–PPO–PEO triblock copolymer (F127, 12 600 g mol^{-1}) was bought from Sigma Aldrich. Chloroform and toluene were purchased from Sinopharm Chemical Reagent Co., Ltd. Carboxylated multiwall carbon nanotubes (CNTs) were obtained from Chengdu Organic Chemicals Co., Ltd. Commercial dispersant (XFZ20) was purchased from Nanjing XFNANO Materials Tech Co., Ltd.

Fabrication of aligned SEBS/F127 fiber films

First of all, SEBS and F127 with different weight ratios were dissolved in a mixed solvent of chloroform and toluene (80/20 wt/wt) with a total concentration of 15 wt%. The solutions were vigorously stirred for 90 min at ambient temperature. Following that, the viscous solutions were transferred to a syringe and mounted on an electrospinning equipment with the process parameters listed as follows: the pumping speed was kept at 10 mL h^{-1} through a 21 G syringe needle, the applied positive voltage was 20 kV and the negative voltage was −2 kV, the distance from the orifice to the collector was 15 cm, and the rotating speed of the drum collector was kept at 2800 rpm. The whole fabrication process was performed in a sealed chamber at 35 °C and 30% relative humidity. Four SEBS/F127 blending ratios (95/5, 90/10, 85/15 and 80/20, wt/wt) were studied to optimize the surface properties and mechanical strength of the elastomer fibers, and the obtained samples were abbreviated as SEBS/F127-5 wt%, SEBS/F127-10 wt%, SEBS/F127-15 wt%, and SEBS/F127-20 wt%, respectively.

Preparation of CNT/SEBS/F127 composite fiber films

The entire fabrication process of anisotropic CNT/SEBS/F127 composite films is schematically depicted in Fig. 1A. Typically, 200 mg dispersant (XFZ20) was first dissolved in 200 mL deionized water at 60 °C, and 1 g CNT powder was subsequently added into the above solution and intermittently sonicated with a cell disruptor for 60 min (Fig. S1†). The electrospun aligned SEBS/F127 fiber films were cut into pieces with a size of 40 × 40 mm^2, which were then soaked in the above CNT dispersion for 30 min in an ultrasonic bath for the complete surface-induced

This journal is © The Royal Society of Chemistry 2021

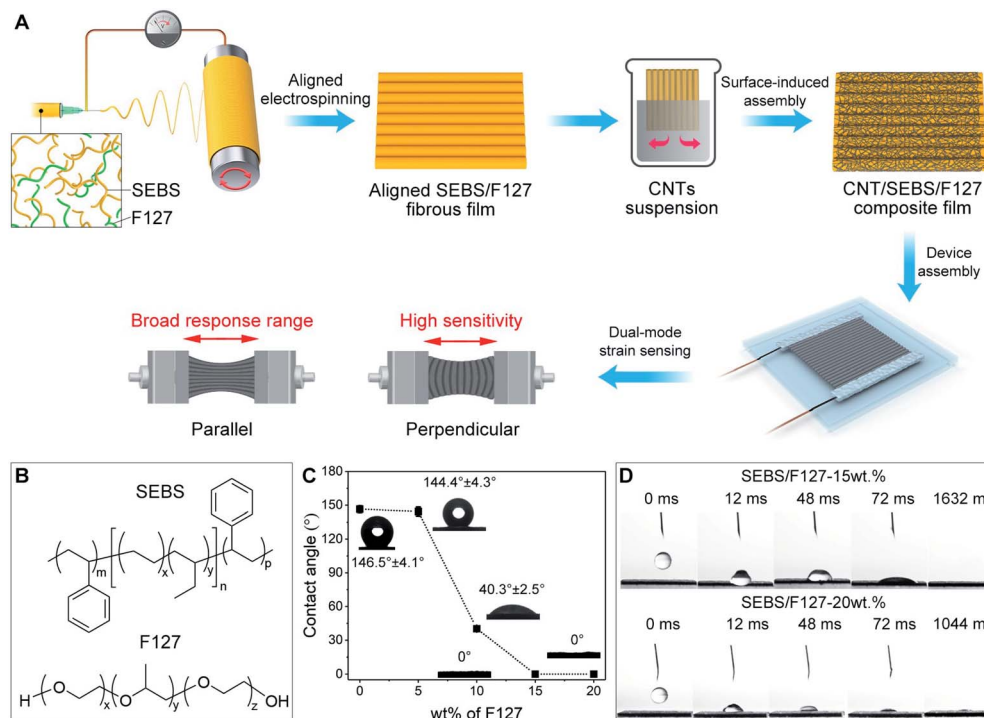*J. Mater. Chem. A*, 2021, **9**, 18294–18305 | **18295**

Fig. 1 (A) Schematic illustration of the preparation process of CNT/SEBS/F127 fiber films. (B) Chemical structures of SEBS and F127. (C) Static water contact angle of SEBS and SEBS/F127 composite films. (D) Dynamic hydrophilic behavior of SEBS/F127-15 wt% and SEBS/F127-20 wt%, respectively.

assembly of acidized CNTs. After that, the wet fiber films were vacuum dried at 60 °C for 6 h to obtain CNT/SEBS/F127 composite fiber films.

Characterization

The morphologies of different fiber films were observed by using a field emission scanning electron microscope (FESEM, Hitachi, S4800). The distribution of elements on the SEBS and SEBS/F127 fiber films was scanned by EDS. Raman spectra were acquired using a 532 nm laser (Renishaw inVia Reflex). Water contact angle measurements were conducted with a Data-physics instrument (OCA15EC). High-speed images of wetting behavior were recorded using an Olympus i-speed3 camera working at 1000 frames per second. Dynamic mechanical properties were measured by using a dynamic mechanical analyzer (DMA, TA Instruments Q800) with a tensile film fixture operating in the strain rate mode. The electromechanical properties of CNT/SEBS/F127 fiber films were investigated with a universal tensile testing machine (UTM2203, Sun Technology Stock Co., Ltd.) coupled with a digital multimeter (Tektronix, DMM 6550 1/2).

Results and discussion

Structural and morphological characterization

SEBS is a kind of triblock copolymer consisting of plastic polystyrene and rubbery polyethylene and polybutylene, which features high stretchability, eco-friendliness, leftover recyclability and excellent processability, and thus recently emerged as a promising candidate for wearable strain sensors. However, the intrinsic superhydrophobic nature of SEBS severely restricts its efficient incorporation with conductive particles such as carbon materials. Hence, F127 was blended with SEBS to modify the surface properties of electrospun elastomer fiber films (the chemical structures of both polymers are shown in Fig. 1B). Water contact angles were first measured to characterize the hydrophilicity of the composite fiber films. As can be observed in Fig. 1C, the pure SEBS film exhibits a completely hydrophobic surface, and this situation barely changed when 5 wt% F127 was blended with SEBS. Interestingly, the contact angle of the composite film undergoes a sharp decline when the F127 mass fraction increases to 10 wt%, and reaches near zero when 15 wt% F127 was blended with SEBS, evidencing the superhydrophilic surface properties of SEBS/F127 fiber films. High-speed imaging equipment was also used to investigate the dynamic absorbing behavior of two superhydrophilic SEBS/F127 samples, i.e., the composite fibers with 15 wt% and 20 wt% F127 (Fig. 1D). Apparently, the contact angles of both films keep declining right after the water drops come into contact with the film, and decrease to near zero until the complete absorption of the droplets at around 1632 ms and 1044 ms for SEBS/F127-15 wt% and SEBS/F127-20 wt%, respectively. The significant difference in the water absorption speed can be readily ascribed to the better hydrophilicity of the 20 wt% F127 sample. The superhydrophilic surface of the composite fiber films stems from the abundant hydroxyl groups in F127, which brings about two main benefits for the SEBS/

18296 | J. Mater. Chem. A, 2021, 9, 18294–18305

This journal is © The Royal Society of Chemistry 2021

F127 fiber films, including strong affinity with electrically conductive CNT particles based on strong interfacial interaction, and good sweat absorption and releasing functions when mounted on textiles.[36]

Upon the incorporation of F127, the shape stability and processability of the electrospun SEBS fiber films were also greatly improved. Since the rubber blocks and hard polystyrene within SEBS are thermodynamically incompatible, strong microphase separation would occur and results in the formation of polystyrene domains, and these domains act as a physical cross and can be ruptured and reset by a combination of shear and temperature. As shown in Fig. 2A, the as-spun pure SEBS fiber films peeled from the receiving roller exhibit an obvious crimping phenomenon owing to the intrinsic phase separation of SEBS, and the poor formability would severely impede the processability and application of pure SEBS fibers. The intertangling behavior of elastomer fiber films is remarkably improved when blended with F127 (Fig. 2A). Especially, composite films with 15 wt% and 20 wt% F127 can be easily flattened, and this can be explained by weakened microphase separation proved by the DMA results. Fig. 2B presents the plots of tan δ (damping factor) *versus* temperature for SEBS and SEBS/F127 composites. The damping factor is the ratio of loss modulus and storage modulus, and reflects the balance between the viscous and elastic phases of polymer composites. Pure SEBS exhibited two glass transition temperatures (T_g) at -32 °C and 79 °C, corresponding to the rubbery (ethylene–butylene) and plastic (styrene) segments, respectively. In contrast, the SEBS/F127 film only possesses one T_g peak of rubbery portions at around -25 °C, revealing that the physical cross is partially ruptured by the steric molecular hindrances of

F127.[37] As a result, the microphase segregation effect was weakened and the formability of the electrospun fiber films was largely enhanced. The shape stability of elastomer films is critical for the homogeneous incorporation of conductive materials and their practical applications for wearable electronics.

Raman spectra provide the fingerprints of vibrational frequencies that correspond to a molecule's chemical bonds and symmetry. In Fig. 2C, Raman bands related to the styrene segment (hard phase) of SEBS can be found at 1603 cm^{-1}, 1001 cm^{-1}, and 620 cm^{-1} attributed to =C–H and –C=CH ring stretching.[38] Moreover, C–H vibrational bands located at 1153 and 1001 cm^{-1} can be assigned to the ethylene–butylene portion (soft phase) of SEBS.[39] As for F127, the weak bands at 845 cm^{-1} and 860 cm^{-1} are attributed to the –CH$_2$ and –CH$_3$ rocking vibrations, and the strong bands at 1230 cm^{-1} and 1282 cm^{-1} are caused by C–C and C–O stretching vibrations.[40] Notably, the overall Raman intensity of SEBS/F127 gradually decreases with increasing the mass fraction of F127 in the SEBS matrix, indicating the homogeneous blending of both elastomers in the composite fibers. The SEM images of SEBS and SEBS/F127 composite fibers produced by aligned electrospinning are shown in Fig. S2,† presenting the homogeneous structure of all samples. It is worth noting that the diameter of the composite fibers decreases drastically with the incorporation of 5 wt% F127, and reaches a mean value of 5.6 μm at a maximum F127 concentration of 20 wt% (Fig. S2K†). A finer fiber diameter results in a larger specific surface area, which will greatly enhance the binding force between carboxylated CNTs and elastomeric fibers. Additionally, elemental mapping results indicate that the O element is evenly distributed on the electrospun fibers after blending with F127 (Fig. S3†), further confirming that F127 and SEBS were homogeneously blended.

The abundant hydroxyl groups and ether bonds in F127 can form strong H-bonding with carboxylated CNTs, and additionally, π–π stacking interactions between CNTs and SEBS are also highly favorable for strong interfacial interaction between conductive nanoparticles, as schematically depicted in Fig. 2D. Hence, a facile ultrasonic-assisted dip-coating process was subsequently employed to realize the surface-induced assembly of acidized CNTs on superhydrophilic SEBS/F127 fiber films. Compared with the smooth and flat surface manifested by the as-spun SEBS/F127 fibers (Fig. 3A and B), the CNT/SEBS/F127 composite fibers exhibit conspicuous hairy morphologies with one dimensional CNTs evenly distributed on the surface of aligned fibers without the existence of aggregation and blocking (Fig. 3C and D). Besides, the pure white SEBS/F127 film turns into homogeneous matt black after CNT coating (inset of Fig. 3A and C), confirming the uniform distribution of conductive carbon nanomaterials on the fiber films. Meanwhile, the CNT/SEBS/F127 composite film still remains superhydrophilic (Fig. S4C†), indicating that the CNT coating has neglectable influence on the surface properties of the elastic films. Further Raman spectra presented in Fig. 3E evidence that the shifts of CNTs at 1590 cm^{-1} (G-band) and 1350 cm^{-1} (D-band) appear clearly in the spectrum of CNT/SEBS/F127, verifying the successful incorporation of graphite-like carbon nanotubes in
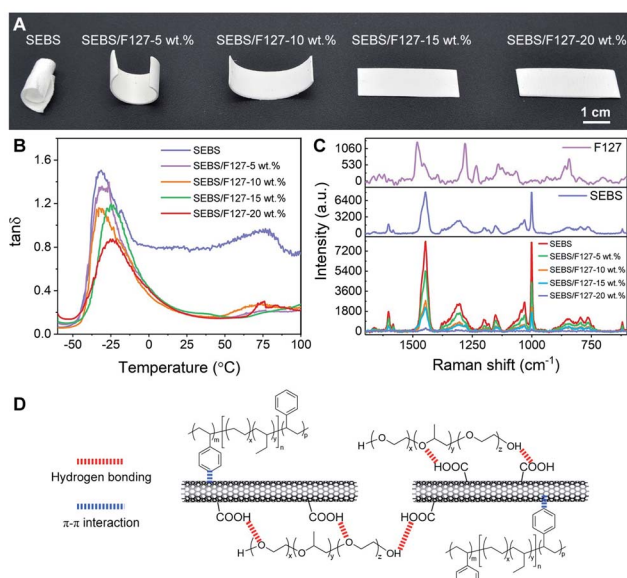

Fig. 2 (A) Digital images and (B) corresponding DMA tests (damping *versus* temperature) of SEBS and SEBS/F127 composite films; (C) Raman spectra of SEBS, F127 and SEBS/F127 composite films. (D) Schematic illustration of the interactions between CNTs and the SEBS/F127 matrix.
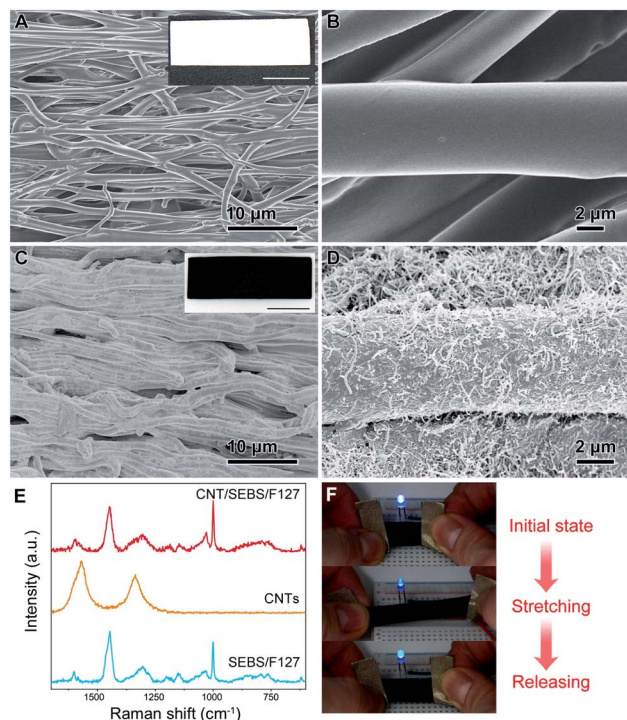
Fig. 3 SEM images of (A and B) the SEBS/F127-15 wt% matrix and (C and D) CNT/SEBS/F127 composite fibers at different magnifications. Insets of (A) and (B): corresponding digital photos of the two samples. (E) Raman spectra of SEBS/F127, CNT and CNT/SEBS/F127 fiber films. (F) A presentation of the electrical conductivity of the CNT/SEBS/F127 fiber film.

the composite film,[32] which could definitely results in terrific conductive paths along the highly aligned elastic fibers. The FTIR spectra in Fig. S4D† also reveal the well-defined peak shift of C–H vibration from 1465 cm^{-1} to 1460 cm^{-1}, plus the slight shift of C–H (benzene ring) bending from 698 cm^{-1} to 700 cm^{-1}, indicating the significant interaction between the SEBS/F127 elastomeric fibers and acidized CNTs. A preliminary demonstration of the variable conductivity was performed by inserting the CNT/SEBS/F127 composite film in a circuit, as displayed in Fig. 3F, and the brightness of the LED can be controlled in real-time through stretching the composite film. The electrospun SEBS fibrous film also underwent an ultrasonic bath treatment in a CNT dispersion for a comparison, as evidenced in Fig. S4A and B,† and most of the area of the SEBS film stays pure white, and there barely exist any CNTs on the aligned fibers under the microscope due to the poor affinity of SEBS elastomeric fibers, highlighting the vital importance of F127 in the composite fiber films.

Tensile properties of the composite fiber films

Reliable mechanical properties of strain sensors are of vital importance for their practical applications. The typical strain–stress curves of SEBS and SEBS/F127 films and their detailed mechanical properties are shown in Fig. 4. When stretching along the parallel direction (tensile direction parallel to the fiber orientation, as indicated in the corner of Fig. 4A), all the

curves exhibit similar shapes with a linear region upon initial stretching, followed by a short plateau when the strain is beyond 1000%, and ended with partial failure (partially torn from one side) and ultimate fracture (Fig. 4A). When tested along the perpendicular direction (tensile direction perpendicular to the fiber orientation), the shapes of the strain–stress curves are similar to the parallel counterparts, except for the absence of partially tearing before the fracture (Fig. 4B). Partial failure usually occurs during the stretching of aligned fiber film materials due to the inevitable slide of fibers under large-scale deformation, as shown in Fig. S5.† In addition, the blending of F127 significantly improves the stretchability of the electrospun SEBS/F127 fiber films in both directions (Fig. 4C); in particular, SEBS/F127-15 wt% possesses the maximum elongation up to about 1600% in the parallel direction, much higher than that of commonly used elastomers like electrospun TPU mats (900%),[41] PDMS films (100%)[42] and wet-spun silicon rubber fibers (300%).[21] The improved stretchability of SEBS fibers may be ascribed to the weakened physical cross of polystyrene after blending with F127, and thus the soft segments are easier to be elongated.[37] Meanwhile, the elongation drastically decreases at an F127 mass fraction of 20 wt%, which is possibly caused by the partial destruction of the polyethylene and polybutene segments (elastic phase). Furthermore, the tensile strength of SEBS and different SEBS/F127 composite fiber films is 2.16 MPa, 1.97 MPa, 1.64 MPa, 2.16 MPa and 2.30 MPa (Fig. 4D), respectively, demonstrating that the blending of F127 has little influence on the strength of the electrospun SEBS fiber films. Strain energy is the work that has been done during the stretching process, which reflects the comprehensive mechanical performance of the material. As can be seen in Fig. 4E, SEBS/F127-15 wt% shows the best mechanical properties in both stretching directions, and thus SEBS/F127-15 wt% was selected as the optimized substrate for strain sensors considering its excellent hydrophilic surface and superior mechanical properties. A further comparison of the tensile properties between isotropic SEBS/F127-15 wt% fiber films (electrospun on a static acceptor with the same polymer composition, Fig. S1B†) and SEBS/F127-15 wt% in different tensile directions was performed (Fig. 4F), and the aligned fiber films in the parallel tensile direction manifest the maximum Young's modulus, tensile strength and strain energy (Fig. S6A–D†), which are 2–3 times greater than those of the isotropic counterpart, demonstrating the great significance of fiber alignment on the mechanical performances. Generally speaking, the Young's modulus of human skin is in the range of 25–220 kPa,[43] which is very close to results obtained for the SEBS/F127 film (148 kPa in the parallel direction and 37 kPa in the perpendicular direction), and thus endows the SEBS/F127 based strain sensor with the capability of detecting subtle skin deformations. The above results demonstrate the excellent mechanical properties and unique anisotropic tensile properties of SEBS/F127 films produced by aligned electrospinning. Such advantages make aligned SEBS/F127 composite films a favorable candidate for the fabrication of strain sensors with an ultra-wide operation range and anisotropic sensing capabilities.
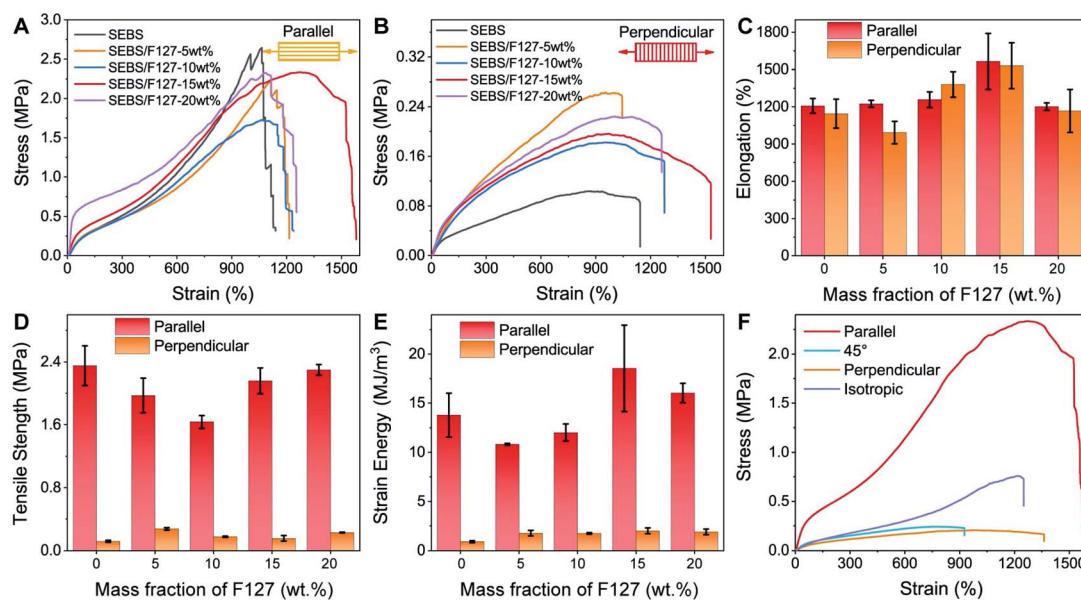
18298 | *J. Mater. Chem. A*, 2021, **9**, 18294–18305

This journal is © The Royal Society of Chemistry 2021

Fig. 4 Typical strain−stress curves of different SEBS/F127 fiber films along (A) parallel and (B) perpendicular directions. (C−E) The elongation, tensile strength and strain energy of different SEBS/F127 fiber films. (F) Strain−stress curves of the SEBS/F127-15 wt% fibrous film in different stretching directions.

The tensile properties of CNT/SEBS/F127 composite fiber films were also investigated in-depth. To begin with, tensile tests of CNT/SEBS/F127 and SEBS/F127 were conducted to investigate the influence of CNT coating. As can be observed in Fig. S7,† there hardly exists any difference in the elongation or breaking strength between CNT/SEBS/F127 and SEBS/F127 films, revealing that the remarkable mechanical performance of electrospun SEBS/F127 is completely preserved. Hysteresis is the ratio of the dissipated energy to the total deformation work (strain energy), and an elastomer with lower hysteresis always exhibits better resilience.[44] The mechanical hysteresis of CNT/SEBS/F127 fiber films in parallel and perpendicular directions was investigated through repetitive stretching and releasing tests for five cycles under micro-deformations from 1% to 10%, and large deformations from 100% to 600%. As shown in Fig. 5, every stress–strain curve consists of a loading curve and an unloading curve, forming a closed loop termed dissipated energy. As for the CNT/SEBS/F127 composite film, energy dissipation basically originated from the internal friction caused by the polymeric chain slipping during the stretching process. The internal friction converts mechanical work into heat energy, resulting in obvious residual strain when the stress is removed. Hence, perfectly overlapped loading/unloading curves reflect the low dissipation energy and high resilience of the elastomeric materials. As shown in Fig. 5A, B, E and F, mechanical hysteresis can hardly be observed at small strains (1%–10%) in both parallel and perpendicular directions. In the case of large strains from 100–600%, the loading/unloading curves in both tensile directions display an obvious hysteresis phenomenon in the first cycle (Fig. 5C, D, G and H), which vanishes rapidly in the next cycles, and remain stable thereafter. The hysteresis weakening is ascribed to the rearrangement of

the composite fibrous network and macromolecular chains according to the Mullins effect.[45] The low hysteresis exhibited by CNT/SEBS/F127 is highly beneficial for the reconstruction of the elastic networks under large deformation, endowing the conductive elastomeric fiber films with great recoverability for strain-sensing applications.

Strain-sensing performance of anisotropic CNT/SEBS/F127 fiber films

Since the CNT/SEBS/F127 fiber films possess remarkable stretchability and toughness, on which uniformly distributed CNT particles can serve as a conducting layer for fast electron transport, their strain-sensing performance in both parallel and perpendicular directions was thoroughly investigated. As can be observed from Fig. 6, the CNT/SEBS/F127 fiber film exhibits fairly stable piezoresistive responses for three successive cycles under various strains in both loading directions, indicating its excellent structural stability and integrated conductive path manifested by the anisotropic composite fibers. It is also notable that the resistance rises gradually with stepwise increasing the applied strain, which is caused by the separation of conductive CNTs during the gradual stretching of the elastic substrates. In the parallel direction, the sensor exhibits a broad strain sensing range up to 1300% (Fig. 6B), and the GF value (the slope of $\Delta R/R_0$ versus strain, where ΔR is the resistance change during stretching tests and R_0 is the initial resistance) reaches 179.8 at the largest applicable strain of 1300%. On the other hand, the film sensor applied in the perpendicular direction achieves an ultra-high maximal GF value of 3564 at a strain of 700%. The relatively decreased sensing range in the perpendicular direction is possibly caused by the sharp shrinkage of the CNT contact area at a large strain. The sensing

This journal is © The Royal Society of Chemistry 2021

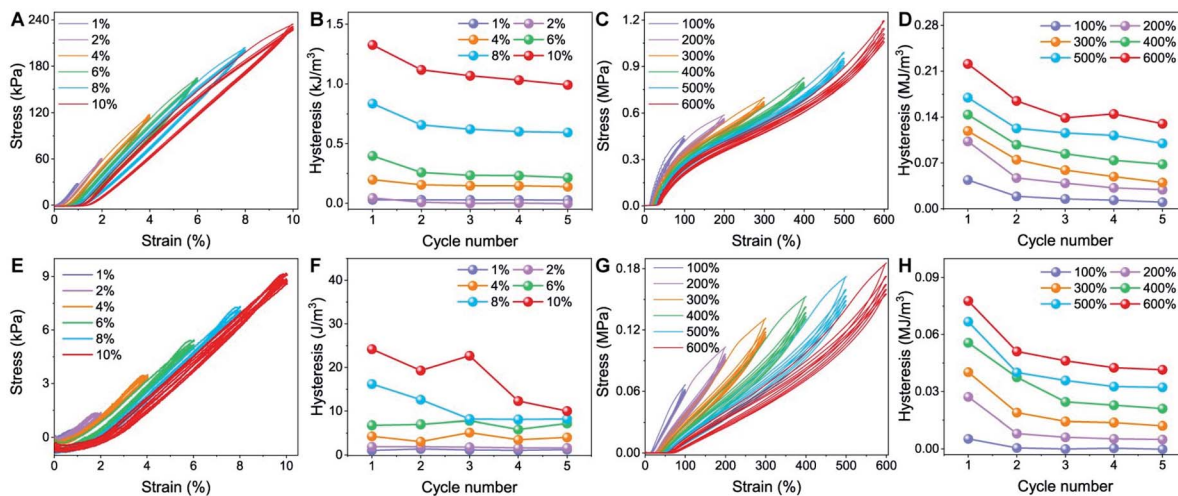*J. Mater. Chem. A*, 2021, **9**, 18294–18305 | **18299**

Fig. 5 Strain–stress curves and corresponding hysteresis of the initial five stretching–releasing cycles of the CNT/SEBS/F127 composite fiber film in (A–D) parallel and (E–H) perpendicular directions in the strain ranges of 1–10% and 100–600%.

ranges and GF values in previously reported related studies are listed in Table 1 for a thorough comparison. Various elastic substrates, conducive layers and fabrication methods are summarized. Notably, crack-based sensors show remarkably high gauge factors, ultralow detection limits and long-term durability;[53–56] however, their maximal detection range is limited. Apparently, the CNT/SEBS/F127 fiber film in this work possesses superior dual-mode strain sensing capability in terms of the widest sensing range and the highest GF values in parallel and perpendicular directions, highlighting the importance of structural design for CNT/SEBS/F127 composite fiber films. Apart from the sensing range and sensitivity, the linear response region is another significant index to evaluate the performance of strain sensors. As clearly demonstrated in

Fig. 6C and F, the $\Delta R/R_0$ *versus* strain plots in both parallel and perpendicular directions exhibit two distinct linear regions. In the parallel direction, the GF value remains at 3.6 within the applied strain of 0–150%, which rises to 18 when the strain is larger than 150% (Fig. 6C). The same scenario occurs in the perpendicular direction, but with much larger GF values than that of parallel sensors under the same deformations (Fig. 6F).

The remarkable anisotropic strain sensing performance is speculated to originate from the structural change of the adaptive deformable CNT layers on highly aligned elastomer fibers. As well-displayed in Fig. 3C and D, uniformly deposited CNTs on SEBS/F127 composite fibers can form a conductive network *via* entangling with each other. Under gentle stretching along the parallel direction (<150% in this case), CNTs adhered
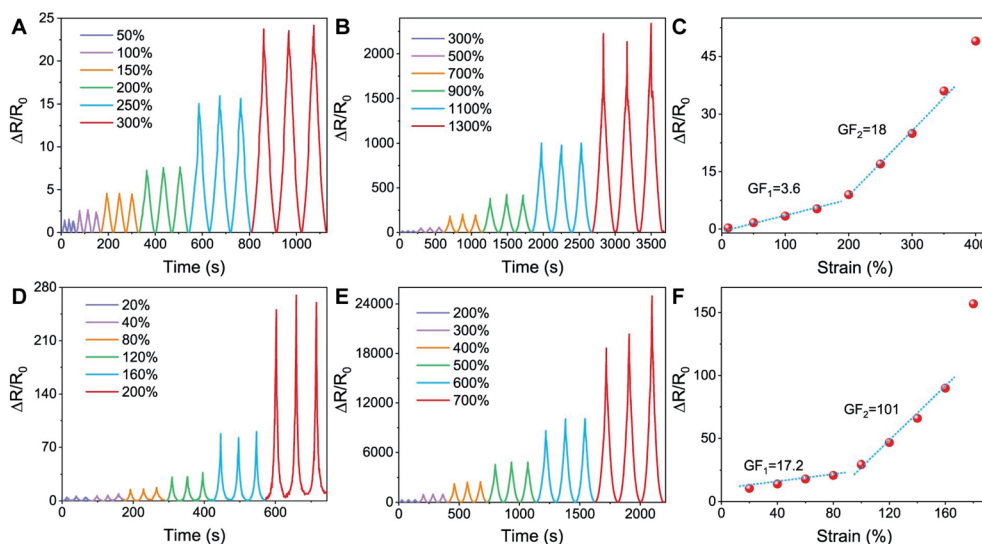

Fig. 6 Relative resistance changes of the anisotropic CNT/SEBS/F127 strain sensor under cyclic stretching–releasing at various tensile strains with the loading direction (A and B) parallel and (D and E) perpendicular to the fiber alignment. Corresponding linear strain-sensing regions in (C) parallel and (F) perpendicular directions.

18300 | *J. Mater. Chem. A*, 2021, **9**, 18294–18305

This journal is © The Royal Society of Chemistry 2021

Table 1 Comparisons of the strain-sensing performance between anisotropic CNT/SEBS/F127 fiber films and recently reported sensors

Matrix	Conductive filler	Maximum range	Maximum GF value	Reference
SEBS/F127 (this work)	Acidized CNTs	1300%	179.8	Parallel
		700%	3564	Perpendicular
PDMS film	AgNWs	35%	>20	15
PDMS film	CNTs	20%	1140	16
PDMS film	CNTs/GNPs	50%	7.04	17
TPU film	Graphene	100%	79	18
TPU fiber	CNTs	320%	97.5	19
TPU mat	AgNWs	200%	338.47	20
PU yarns	GNPs/CBs/CNTs	350%	2.14	46
TPU nanofibers	MXene	110%	9540	47
DI/Ecoflex	Graphene	400%	31.6	22
Ecoflex fibers	CNTs	600%	1378	21
Rubber/PDMS	Carbon black	980%	242.6	12
SEBS film	Graphene/black phosphorus	20%	2765	48
SEBS filament	CNTs	250%	17.36	13
SEBS fiber	Few-layered graphene	110%	546	49
3D printed PLA strip	CNTs	95%	1342	50
Nonwoven fabric	Graphene	98%	2.36×10^4	51
Ionic hydrogels	Ag NFs	1000%	165	52
SiC-based strain sensor	SiC	5%	2.47×10^5	53
AIE sensor	CNTs	>100%	1665.9	54
Carbonized leather	Carbon flake	~3%	2009.5	55
UV/O$_3$-cracked strain sensor	CNTs	100%	1020.2	56

to the fiber surface only slip away with one another, leaving the conductive network intact, thus leading to the slow increase of resistance and a low GF value (~3.6),[47,57] as shown in Fig. 7A (100% strain). When a larger strain is exerted (≥200%), the intimate connection between CNT particles stuck to the fiber surface tends to separate gradually along with the large-scale stretching of SEBS/F127 matrices, and thus the interconnected conductive network for electron transport is significantly restricted, resulting in the sharp increase of resistance and a higher GF value (~18). Additionally, the SEM images of the CNT/SEBS/F127 composite film under various strains reveal that the fiber alignment significantly enhances under stretching (Fig. 7A–F), resulting in a complete electrical contact between individual fibers (as vividly illustrated in Fig. 7M), thus endowing the parallel CNT/SEBS/F127 sensor with an ultrabroad sensing range up to 1300%. The structural evolution of the anisotropic conducting film is totally different when stretching along the perpendicular direction. As clearly presented in Fig. 7G–I, the composite fibers easily detach from one another when a minor strain is applied perpendicular to the fiber alignment, and thus larger sensitivity can be achieved under the same deformation as stretching in parallel. When gradually increasing the external strain beyond 500%, the vast majority of the well-contact fibers are detached from each other (Fig. 7K and L), leaving few CNT/SEBS/F127 fibers serving as bridging units to sustain the conducting path *via* a limited electrical contact (Fig. 7M), thus endowing the perpendicular strain sensor with an extraordinary GF value of 3564 at a strain of 700%. As response sensitivity determines the effectiveness of wearable sensors, the as-obtained anisotropic sensor is expected to have great potential in monitoring human motions. Especially, there barely exists any breakage or cracks on the
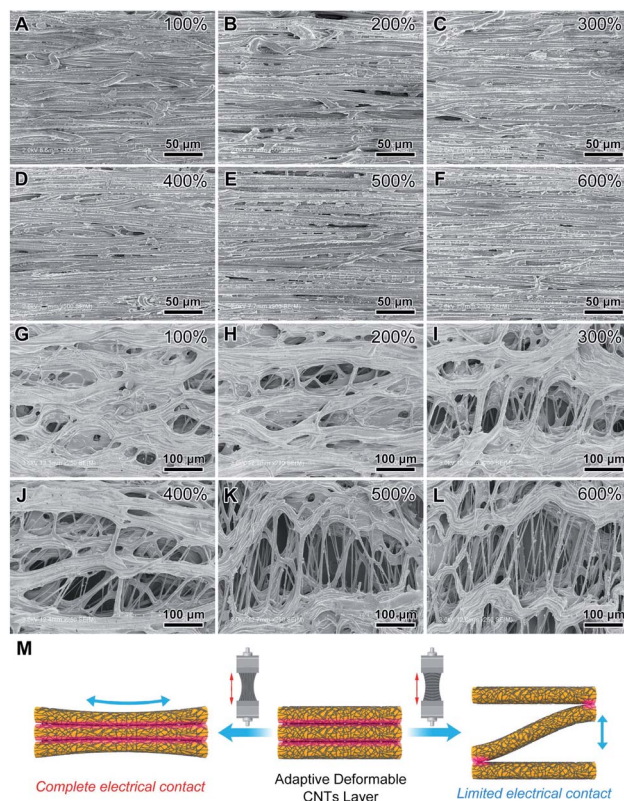

Fig. 7 SEM images of CNT/SEBS/F127 composite fibers stretched in (A–F) parallel and (G–L) perpendicular directions under a stepwise increase of strains from 100% to 600%. (M) Schematic showing the adaptive deformation of the CNT layer on the SEBS/F127 fibers during stretching in parallel and perpendicular directions.

This journal is © The Royal Society of Chemistry 2021

J. Mater. Chem. A, 2021, **9**, 18294–18305 | **18301**

fiber surface in both stretching directions, revealing the exceptional deformability and structural adaptivity of the CNT conducting layer, which are absolutely attributed to the strong interfacial interaction between acidized CNTs and the hydrophilized elastomer fibers. As schematically illustrated in Fig. 7M, the adaptive deformable CNT layer constructed from interweaved carbon nanotubes is able to stretch and recover synchronously with the large-scale deformation of the elastic matrix, thus resulting in the superior dual-mode strain sensing performance of CNT/SEBS/F127 composite fiber films.

A stable response at multiple stretching rates is also very critical for the practical applications of strain sensors under complex conditions. As shown in Fig. 8A and B, the resistance responses of the anisotropic strain senor at a series of tensile rates (50–100 mm min^{-1}) were evaluated within linear regions. Obviously, the stable maximum response at all tensile rates evidences that the sensing behavior of the CNT/SEBS/F127 anisotropic sensor in both parallel and perpendicular directions is not affected by stretching rates, which is beneficial for acquiring reliable strain signals under intricate working conditions. The anisotropic detection limits were also determined, as shown in Fig. S8,† and the parallel CNTs/SEBS/F127 sensor shows a minimal detection of 1.5% while the perpendicular direction reaches a lower value of 0.5%. Further tests were conducted under a slight strain stimulus at a high tensile rate (100 mm min^{-1}) to investigate the response and recovery time of the anisotropic strain sensor towards tiny deformation. Encouragingly, the parallel strain sensor manifests a very fast response and recovery time of 51 ms and 71 ms under 1.5% strain (Fig. 8B), and the excellent responsiveness of the strain sensor can facilitate its application in the real-time monitoring of complex physiological signals such as subtle muscle motion, breathing and swallowing. Furthermore, the perpendicular strain sensor tested under 0.5% strain exhibits a relatively longer response and recovery time of 100 ms and 100 ms,

respectively, coupled with an inconspicuous "shoulder peak" located at the end of the unloading process (Fig. 8E). The possible causes for the emergence of the shoulder peak in the perpendicular direction may be ascribed to the mechanical hysteresis of the elastic matrix and the competition between the destruction and reconstruction of the conductive path during cyclic stretching and releasing.[58,59] Long-term response stability is also very crucial for the practical applications of strain sensors. The durability and stability of the CNT/SEBS/F127 anisotropic sensor in both parallel and perpendicular directions are investigated by recording the resistance under cyclic stretching–releasing. As depicted in Fig. 8C and F, the dual-mode strain sensor shows remarkable long-term durability and stability in both directions even up to 5000 cycles. In addition, the peak and valley $\Delta R/R_0$ values in selected cycles (1000th and 4000th) witness no change after long-term deformation, further displaying the outstanding response stability of the as-prepared anisotropic strain sensor.

Considering the combined advantages of an ultra-broad workable range, high sensitivity, low response time and superior stability, the as-fabricated anisotropic CNT/SEBS/F127 strain sensor is expected to be used as a wearable sensor to monitor multiple human motions. As schematically shown in Fig. 9A, the assembled flexible strain sensor was attached to the wrist, finger, and elbow joints of the human body to monitor large motion signals in real time. As expected, the wearable strain sensor responds rapidly and repeatedly against the wrist motions in both working directions. Specifically, the perpendicular sensor exhibits a much larger resistance change than the parallel sensor under the same strain (Fig. 9B); furthermore, when the CNT/SEBS/F127 sensor was mounted on the knee joint, the perpendicular working mode outputs much intense resistance variation than the parallel mode at various bending angles (Fig. 9C and D), highlighting the unique anisotropic characteristics of the designed strain sensor. Hence, the
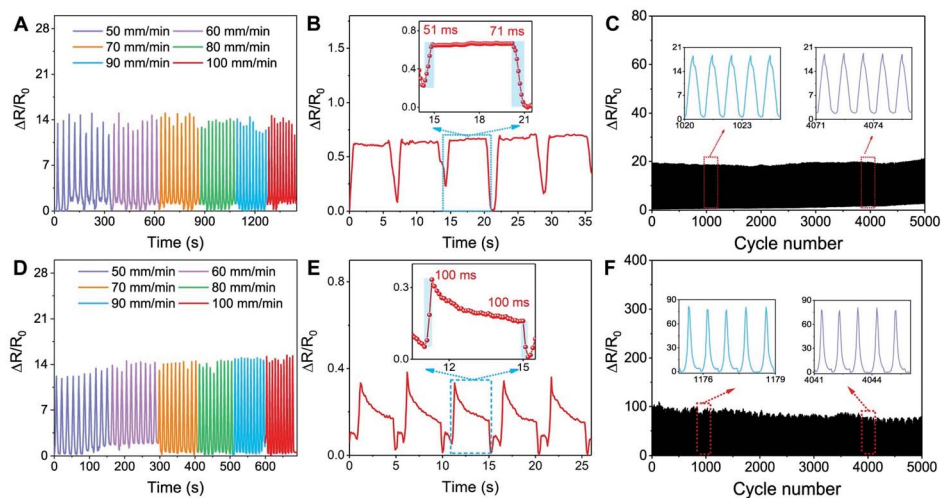

Fig. 8 Relative resistance changes of the CNT/SEBS/F127 strain sensor under cyclic stretching–releasing at various tensile speeds (50–100 mm min^{-1}): (A) parallel direction under a strain of 250% and (D) perpendicular direction under a strain of 40%. Response/recovery time of the sensor in (B) parallel and (E) perpendicular directions. Cycling stability tests of the sensor in (C) the parallel direction under a strain of 250% and (F) the perpendicular direction under a strain of 150%.
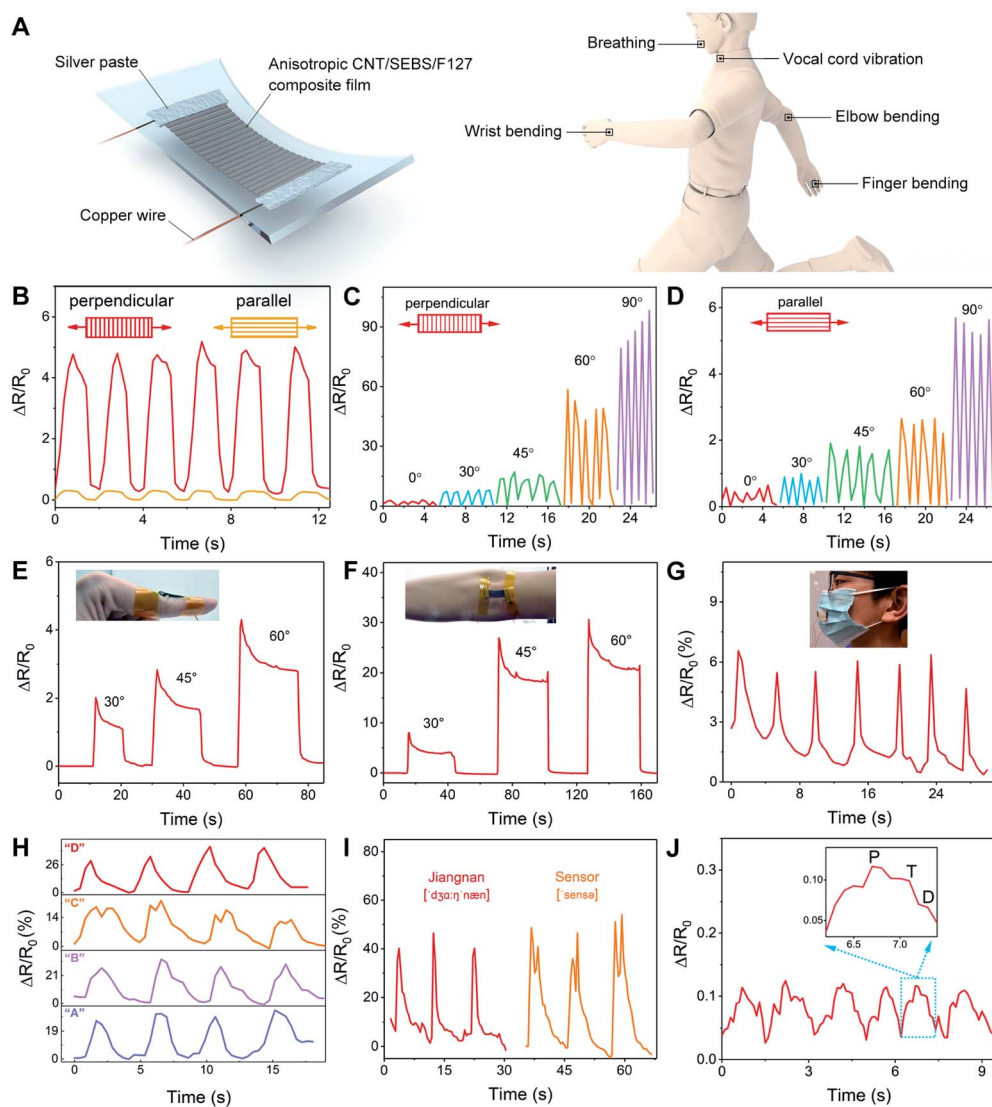
18302 | J. Mater. Chem. A, 2021, 9, 18294–18305

This journal is © The Royal Society of Chemistry 2021

Fig. 9 Real-time monitoring of small and large human motions using the anisotropic CNT/SEBS/F127 film sensor: (A) schematic illustrations for the configuration of the wearable sensor, and the sensor attached to various parts of the human body for signal acquisition. Resistance signals of the CNT/SEBS/F127 anisotropic strain sensor in different working modes: (B) wrist bending and (C and D) knee joint bending at various angles. Resistance signals of the anisotropic strain sensor in perpendicular working mode: (E and F) finger and elbow bending at different angles, (G) breath detection, (H) phonation of letters "A–D" and (I) words "Jiangnan" and "Sensor", and (J) wrist pulse detection.

following motion detection experiments were carried out with the CNT/SEBS/F127 sensor assembled in the perpendicular orientation. Fig. 9E and F present the sharp on–off resistance signals of finger and elbow bending at different angles of 30°, 45° and 60°, and clearly, the resistance increases with increasing the bending angle due to the stretching of the composite fiber. Owing to the fast response and recover ability, the strain sensor is able to instantly reflect the joint bending, and returns to its initial state when the finger and elbow straighten. Furthermore, the device was attached to a mask to capture the micro-expansion of the mask during breathing, and the high sensitivity and stability of the sensor are also reflected by the sharp peaks in Fig. 9G. Apart from these, micro-motions such as vocal cord vibration was also monitored *via* attaching the CNT/SEBS/F127 strain sensor to the human throat. As shown in Fig. 9H, stable resistance responses are generated

when speaking different letters "ABCD". Even more, the pronunciation of different words "Jiangnan" and "Sensor" is also distinguished by well-defined signals (Fig. 9I). Subtle deformation like wrist pulses was monitored to examine the sensibility of the sensor, and it can be observed from Fig. 9J that the signal of the radial artery shows three well-defined characteristic P, T and D peaks. Therefore, the anisotropic CNT/SEBS/F127 composite fiber film-based strain sensor may have great potential applications in monitoring human motion and health in real time.

Conclusion

In summary, a rationally designed anisotropic CNT/SEBS/F127 strain sensor was fabricated *via* surface-induced assembly of acidized CNTs on highly aligned SEBS/F127 elastic fiber films.

Owing to the remarkable mechanical properties of the highly stretchable SEBS/F127 film and the strong interfacial interaction between interweaved CNTs and the superhydrophilic fiber matrix, the as-designed CNT/SEBS/F127 equipped with an adaptive deformable CNT conducting layer exhibited distinguished dual-mode strain sensing capabilities in terms of an ultra-wide strain-sensing range of 1300% in the parallel direction, and a high gauge factor up to 3564 at a strain of 700% in the perpendicular direction, which also manifests prominent real-time detection ability towards human motions, making this CNT/SEBS/F127 anisotropic strain sensor a promising candidate in wearable and flexible strain sensors.

Conflicts of interest

The authors declare no conflict of interest.

Acknowledgements

References

1 H. Kim, Y.-T. Kwon, H.-R. Lim, J.-H. Kim, Y.-S. Kim and W.-H. Yeo, *Adv. Funct. Mater.*, 2020, 2005692.

2 J. Lee, B. Llerena Zambrano, J. Woo, K. Yoon and T. Lee, *Adv. Mater.*, 2020, **32**, 1902532.

3 Y. Niu, H. Liu, R. Y. He, Z. D. Li, H. Ren, B. Gao, H. Guo, G. M. Genin and F. Xu, *Mater. Today*, 2020, **41**, 219–242.

4 D. Suh, K. P. Faseela, W. Kim, C. Park, J. G. Lim, S. Seo, M. K. Kim, H. Moon and S. Baik, *Nat. Commun.*, 2020, **11**, 2252.

5 N. Matsuhisa, X. Chen, Z. Bao and T. Someya, *Chem. Soc. Rev.*, 2019, **48**, 2946–2966.

6 H. Jin, M. O. G. Nayeem, S. Lee, N. Matsuhisa, D. Inoue, T. Yokota, D. Hashizume and T. Someya, *ACS Nano*, 2019, **13**, 7905–7912.

7 W. S. Meng, M. Y. Nie, Z. Y. Liu and J. Zhou, *Adv. Fiber Mater.*, 2021, **3**, 149–159.

8 C. H. Deng, L. F. Lan, P. H. He, C. C. Ding, B. Z. Chen, W. Zheng, X. Zhao, W. S. Chen, X. Z. Zhong, M. Li, H. Tao, J. B. Peng and Y. Cao, *J. Mater. Chem. C*, 2020, **8**, 5541–5546.

9 J. G. Sun, H. Y. Guo, J. Ribera, C. S. Wu, K. K. Tu, M. Binelli, G. Panzarasa, F. W. M. R. Schwarze, Z. L. Wang and I. Burgert, *ACS Nano*, 2020, **14**, 14665–14674.

10 J. G. Sun, H. Z. Guo, G. N. Schädli, K. K. Tu, S. Schär, F. W. M. R. Schwarze, G. Panzarasa, J. Ribera and I. Burgert, *Sci. Adv.*, 2021, **7**, eabd9138.

11 H. Li, J. W. Chen, X. H. Chang, Y. Q. Xu, G. Y. Zhao, Y. T. Zhu and Y. J. Li, *J. Mater. Chem. A*, 2021, **9**, 1795–1802.

12 Y. Chen, L. Wang, Z. F. Wu, J. C. Luo, B. Li, X. W. Huang, H. G. Xue and J. F. Gao, *Composites, Part B*, 2019, **176**, 107358.

13 X. H. Cui, Y. Jiang, Z. G. Xu, M. Xi, Y. Jiang, P. A. Song, Y. Zhao and H. Wang, *Composites, Part B*, 2021, **211**, 108641.

14 Z. Lv, X. Huang, D. Y. Fan, P. Zhou, Y. Y. Luo and X. X. Zhang, *Compos. Commun.*, 2021, **25**, 100685.

15 K. K. Kim, S. Hong, H. M. Cho, J. Lee, Y. D. Suh, J. Ham and S. H. Ko, *Nano Lett.*, 2015, **15**, 5240–5247.

16 B. B. Nie, X. M. Li, J. Y. Shao, X. Li, H. M. Tian, D. R. Wang, Q. Zhang and B. H. Lu, *ACS Appl. Mater. Interfaces*, 2017, **9**, 40681–40689.

17 F. Zhang, S. Y. Wu, S. H. Peng, Z. Sha and C. H. Wang, *Compos. Sci. Technol.*, 2019, **172**, 7–16.

18 Y. Wang, J. Hao, Z. Q. Huang, G. Q. Zheng, K. Dai, C. T. Liu and C. Y. Shen, *Carbon*, 2018, **126**, 360–371.

19 X. Z. Wang, H. L. Sun, X. Y. Yue, Y. F. Yu, G. Q. Zheng, K. Dai, C. T. Liu and C. Y. Shen, *Compos. Sci. Technol.*, 2018, **168**, 126–132.

20 Y. Huang, X. Y. You, X. Y. Fan, C. P. Wong, P. Guo and N. Zhao, *Adv. Mater. Technol.*, 2020, **5**, 2000550.

21 Z. H. Tang, S. H. Jia, F. Wang, C. S. Bian, Y. Y. Chen, Y. L. Wang and B. Li, *ACS Appl. Mater. Interfaces*, 2018, **10**, 6624–6635.

22 M. X. Xu, J. J. Qi, F. Li and Y. Zhang, *Nanoscale*, 2018, **10**, 5264–5271.

23 X. X. Li, J. Z. Yang, W. J. Yuan, P. G. Ji, Z. B. Xu, S. N. Shi, X. J. Han, W. X. Niu and F. X. Yin, *Compos. Commun.*, 2021, **23**, 100586.

24 H. J. Zhang, W. Q. Han, K. Xu, H. J. Lin, Y. F. Lu, H. D. Liu, R. Z. Li, Y. H. Du, Z. T. Nie, F. Xu, L. Miao, J. X. Zhu and W. Huang, *Adv. Funct. Mater.*, 2021, **31**, 2009466.

25 L. Li, Y. Zhang, H. Y. Lu, Y. F. Wang, J. S. Xu, J. X. Zhu, C. Zhang and T. X. Liu, *Nat. Commun.*, 2020, **11**, 62.

26 Y. C. Cai, J. Shen, C.-W. Yang, Y. Wan, H.-L. Tang, A. A. Aljarb, C. L. Chen, J.-H. Fu, X. Wei, K.-W. Huang, Y. Han, S. J. Jonas, X. C. Dong and V. Tung, *Sci. Adv.*, 2020, **6**, eabb5367.

27 Q. Gao, P. Wang, M. X. Wang, Y. H. Wang and J. D. Zhu, *Compos. Commun.*, 2021, **25**, 100700.

28 T. N. Lam, G. S. Lee, B. Kim, H. Dinh Xuan, D. Kim, S. I. Yoo and J. Yoon, *Compos. Sci. Technol.*, 2021, **210**, 108811.

29 Z. Yang, D.-Y. Wang, Y. Pang, Y.-X. Li, Q. Wang, T.-Y. Zhang, J.-B. Wang, X. Liu, Y.-Y. Yang, J.-M. Jian, M.-Q. Jian, Y.-Y. Zhang, Y. Yang and T.-L. Ren, *ACS Appl. Mater. Interfaces*, 2018, **10**, 3948–3954.

30 J. F. Gao, L. Wang, Z. Guo, B. Li, H. Wang, J. C. Luo, X. W. Huang and H. G. Xue, *Chem. Eng. J.*, 2020, **381**, 122778.

31 Y. Y. Jia, X. Y. Yue, Y. L. Wang, C. Yan, G. Q. Zheng, K. Dai, C. T. Liu and C. Y. Shen, *Composites, Part B*, 2020, **183**, 107696.

32 S. Chen, Y. J. Song, D. Q. Ding, Z. Ling and F. Xu, *Adv. Funct. Mater.*, 2018, **28**, 1802547.

33 F. Fang, Y.-Q. Li, G.-W. Huang, H.-M. Xiao, Q.-P. Feng, N. Hu and S.-Y. Fu, *RSC Adv.*, 2017, **7**, 4260–4268.

34 S. Ryu, P. Lee, J. B. Chou, R. Xu, R. Zhao, A. J. Hart and S.-G. Kim, *ACS Nano*, 2015, **9**, 5929–5936.

35 Z. H. Zeng, S. I. Seyed Shahabadi, B. Y. Che, Y. F. Zhang, C. Y. Zhao and X. H. Lu, *Nanoscale*, 2017, **9**, 17396–17404.

18304 | *J. Mater. Chem. A*, 2021, **9**, 18294–18305

This journal is © The Royal Society of Chemistry 2021

36 W. Gong, X. L. Wang, W. F. Yang, J. Zhou, X. Han, M. D. Dickey, Y. Su, C. Y. Hou, Y. G. Li, Q. H. Zhang and H. Z. Wang, *Adv. Mater.*, 2021, **33**, 2007352.

37 M. Pantoja, P.-Z. Jian, M. Cakmak and K. A. Cavicchi, *ACS Appl. Polym. Mater.*, 2019, **1**, 414–424.

38 C. M. De León-Almazán, I. A. Estrada-Moreno, J. L. Olmedo-Martínez and J. L. Rivera-Armenta, *Synth. Met.*, 2020, **268**, 116460.

39 D. M. Chipara, D. M. Panaitescu, K. Lozano, R. A. Gabor, C. A. Nicolae and M. Chipara, *Polymer*, 2019, **176**, 74–88.

40 C. Guo, H. Z. Liu, J. Wang and J. Y. Chen, *J. Colloid Interface Sci.*, 1999, **209**, 368–373.

41 M. N. Ren, Y. Zhou, Y. Wang, G. Q. Zheng, K. Dai, C. T. Liu and C. Y. Shen, *Chem. Eng. J.*, 2019, **360**, 762–777.

42 G. Z. Shen, B. H. Chen, T. L. Liang, Z. H. Liu, S. R. Zhao, J. Y. Liu, C. Zhang, W. J. Yang, Y. L. Wang and X. He, *Adv. Electron. Mater.*, 2020, **6**, 1901360.

43 R. Chen, X. Xu, D. Yu, C. Xiao, M. Liu, J. Huang, T. Mao, C. Zheng, Z. Wang and X. Wu, *J. Mater. Chem. C*, 2018, **6**, 11193–11201.

44 M. Fu, J. M. Zhang, Y. M. Jin, Y. Zhao, S. Y. Huang and C. F. Guo, *Adv. Sci.*, 2020, **7**, 2000258.

45 H. Cho, S. Mayer, E. Pöselt, M. Susoff, P. J. in 't Veld, G. C. Rutledge and M. C. Boyce, *Polymer*, 2017, **128**, 87–99.

46 Y. Huang, Y. N. Zhao, Y. Wang, X. H. Guo, Y. Y. Zhang, P. Liu, C. X. Liu and Y. G. Zhang, *Smart Mater. Struct.*, 2018, **27**, 035013.

47 J. Z. Yang, Y. Xu, Y. Y. Song, G. K. Wang, F. X. Yin, H. T. Liu and W. J. Yuan, *Composites, Part A*, 2021, **141**, 106223.

48 A. Chhetry, S. Sharma, S. C. Barman, H. Yoon, S. Ko, C. Park, S. Yoon, H. Kim and J. Y. Park, *Adv. Funct. Mater.*, 2021, **31**, 2007661.

49 X. P. Wang, S. Meng, M. Tebyetekerwa, Y. L. Li, J. Pionteck, B. Sun, Z. Y. Qin and M. F. Zhu, *Composites, Part A*, 2018, **105**, 291–299.

50 S. Mousavi, D. Howard, F. Zhang, J. Leng and C. H. Wang, *ACS Appl. Mater. Interfaces*, 2020, **12**, 15631–15643.

51 H. Liu, Q. M. Li, Y. B. Bu, N. Zhang, C. F. Wang, C. F. Pan, L. W. Mi, Z. H. Guo, C. T. Liu and C. Y. Shen, *Nano Energy*, 2019, **66**, 104143.

52 H. H. Xu, Y. Lv, D. X. Qiu, Y. J. Zhou, H. X. Zeng and Y. C. Chu, *Nanoscale*, 2019, **11**, 1570–1578.

53 Y. Gao, Q. Li, R. Wu, J. Sha, Y. Lu and F. Xuan, *Adv. Funct. Mater.*, 2019, **29**, 1806786.

54 S. Chen, R. Wu, P. Li, Q. Li, Y. Gao, B. Qian and F. Xuan, *ACS Appl. Mater. Interfaces*, 2018, **10**, 37760–37766.

55 Z. Wang, B. Chen, S. Sun, L. Pan and Y. Gao, *Adv. Electron. Mater.*, 2020, **6**, 2000549.

56 Q. Li, K. Wang, Y. Gao, J. P. Tan, R. Y. Wu and F. Z. Xuan, *Appl. Phys. Lett.*, 2018, **112**, 263501.

57 C. X. Tan, Z. G. Dong, Y. H. Li, H. G. Zhao, X. Y. Huang, Z. C. Zhou, J.-W. Jiang, Y.-Z. Long, P. K. Jiang, T.-Y. Zhang and B. Sun, *Nat. Commun.*, 2020, **11**, 3530.

58 S. D. Zhang, K. Sun, H. Liu, X. Y. Chen, Y. J. Zheng, X. Z. Shi, D. B. Zhang, L. W. Mi, C. T. Liu and C. Y. Shen, *Chem. Eng. J.*, 2020, **387**, 124045.

59 B. Li, J. C. Luo, X. W. Huang, L. W. Lin, L. Wang, M. J. Hu, L. C. Tang, H. G. Xue, J. F. Gao and Y.-W. Mai, *Composites, Part B*, 2020, **181**, 107580.

This journal is © The Royal Society of Chemistry 2021

J. Mater. Chem. A, 2021, **9**, 18294–18305 | **18305**